Nonperfused Retinal Capillaries—A New Method Developed on OCT and OCTA

Min Gao,[1,2] Yukun Guo,[1,2] Tristan T. Hormel,[2] Jie Wang,[2] Elizabeth White,[2] Dong-Wouk Park,[2] Thomas S. Hwang,[2] Steven T. Bailey,[2] and Yali Jia[1,2]

[1]Department of Biomedical Engineering, Oregon Health & Science University, Portland, Oregon, United States
[2]Casey Eye Institute, Oregon Health & Science University, Portland, Oregon, United States

PURPOSE. This study aims to develop a new method to quantify nonperfused retinal capillaries (NPCs) and evaluate NPCs in eyes with AMD and diabetic retinopathy (DR).

METHODS. We averaged multiple registered optical coherence tomography (OCT)/OCT angiography (OCTA) scans to create high-definition volumes. The deep capillary plexus slab was defined and segmented. A developed deep learning denoising algorithm removed tissue background noise from capillaries in en face OCT/OCTA. The algorithm segmented NPCs by identifying capillaries from OCT without corresponding flow signals in OCTA. We then investigated the relationships between NPCs and known features in AMD and DR.

RESULTS. The segmented NPC achieved an accuracy of 88.2% compared to manual grading of NPCs in DR. Compared to healthy controls, both the mean number and total length (mm) of NPCs was significantly increased in AMD and DR eyes ($P < 0.001$, $P < 0.001$). Compared to early and intermediate AMD, the number and total length of NPCs were significantly higher in advanced AMD (number: $P < 0.001$, $P < 0.001$; total length: $P = 0.002$, $P = 0.003$). Geography atrophy, macular neovascularization, drusen volume, and extrafoveal avascular area (EAA) significantly correlated with increased NPCs ($P < 0.05$). In DR eyes, NPCs correlated with the number of microaneurysms and EAA ($P < 0.05$). The presence of fluid did not significantly correlate with NPCs in AMD and DR.

CONCLUSIONS. A deep learning-based algorithm can segment and quantify retinal capillaries that lack flow using colocalized OCT/OCTA. This new biomarker may be useful in AMD and DR in predicting progression of these diseases.

Keywords: nonperfused retinal capillaries, OCT, OCTA, deep learning

Optical coherence tomography (OCT) is a noninvasive imaging technique that captures detailed cross-sectional images of retina.[1] Expanding on this technology, OCT angiography (OCTA) provides functional assessment by visualizing blood flow (functional circulation) within the retinal microvasculature.[2] A single OCTA scan produces co-registered OCT and OCTA volumes, enabling the simultaneous extraction of both retinal structural and angiographic features. Retinal fluid and microaneurysms on OCT,[3,4] along with retinal avascular areas on OCTA,[5–8] are typical lesions of diabetic retinopathy (DR). Geography atrophy (GA) and drusen on OCT,[9–13] macular neovascularization (MNV) on OCTA[14] are characteristic features of AMD. The accurate identification and segmentation of these features from OCT/OCTA can potentially stratify DR and AMD severity and predict the progression of a variety of eye diseases, informing clinical management strategies.[15–18]

In diabetic retinopathy, sections of capillaries lose pericytes and endothelium, becoming acellular basement membrane tubes as seen in histopathologic studies. These tubules do not have lumens and correlate to areas of nonperfusion on angiography.[19–21] Combining OCT and OCTA signals allows in vivo quantification of these occluded capillaries. This approach has advantages over previous approaches to measure ischemia such as measurement of avascular areas, vessel density, or fractal dimensions. There are variations in normal intercapillary space, particularly around the foveal avascular zone (FAZ), where nonperfusion is most consequential but may not be helpful in distinguishing disease from control because of this variation. This approach also avoids the false detection of ischemia caused by low signal artifacts due to media opacities or low signal.[6]

There are additional pathologic mechanisms that cause capillaries to have reduced perfusion. In diabetes, an increase in diacylglycerol concentration activates various forms of protein kinase, which sensitize the contractile mechanism of the retinal arteriole, resulting in hypoperfusion. This may be an important pathophysiologic change, especially in early stage of the disease.[22]

In age-related macular degeneration, recent OCTA-based studies have reported changes in retinal capillary perfu-

sion in both dry AMD[9] and wet AMD.[23] Although it is primarily a disease of the outer retina and the choroid, decreased perfusion in the inner retina and deep vascular plexus may result from photoreceptor degeneration.[9,23,24] It is also possible that the retinal vasculature plays a role in the progression of disease.[9,23,25]

A previous study used adaptive optics scanning light ophthalmoscope (AOSLO) infrared structural and fluorescein angiographic paired images to detect nonperfused retinal capillaries (NPCs).[26] However, AOSLO limited the study to the fovea only and NPCs were demonstrated in healthy controls through visual comparison side by side. AOSLO is not a volumetric imaging modality and so cannot inform our understanding of NPC distribution within the various retinal tissue layers. Lynch et al. visualized NPCs by comparing contrast-inverted en face OCT and OCTA, produced by ten-averaged 3 × 3 mm scans centered at the fovea.[27] The en face OCT provided structural capillary information whereas the en face OCTA displayed flow signal within them. By comparing these two modalities, NPC segments in DR at the innermost border of the FAZ were identified. Despite this earlier observation, the automatic identification and segmentation of capillary structures in en face OCT remains challenging because of the low contrast inherent in these images.

Deep learning has proven to be a powerful method for extracting features from biomedical images for super-resolution reconstruction,[28–30] lesion detection, and segmentation.[11,31–34] In this study, we designed a deep learning-based method to denoise en face OCT/OCTA and automatically segment NPCs from paired OCT and OCTA information. The extent and distribution of NPCs were evaluated for healthy eyes and eyes with AMD and DR. We also explored the relationship between NPCs and known AMD and DR biomarkers.

METHODS

Data Acquisition

The Institutional Review Board of Oregon Health & Science University approved this study. Informed consent was obtained from all participants, and the study adhered to the Declaration of Helsinki. The inclusion criteria for the control group required participants to have no history of retinal diseases, hypertension, or diabetes. AMD participants could not have other retinal diseases or previous intraocular surgery, except for cataract surgery. Patients with hypertension were included in the AMD group, as hypertension is common in the elderly and may coexist with AMD. For the DR groups, the inclusion criteria required participants to have a confirmed diagnosis of DR, ranging from mild to moderate nonproliferative DR (NPDR), based on clinical examination. Participants were excluded if they had a history of any other macular diseases, such as epiretinal membrane or vitreomacular traction syndrome.

Six 3 × 3 mm macular OCT/OCTA scans with a 400 × 400-pixel transverse sampling density from one and only one eye of each participant were obtained continuously within 5 minutes using a commercial 120-kHz spectral-domain OCT system (Solix; Visionix USA, Lombard, IL, USA). The split-spectrum amplitude-decorrelation angiography algorithm implemented in this instrument was used to generate the OCTA data.[2] Twelve of the orthogonal scans (x-fast and y-fast) were registered to generate six motion-free

volumes.[35] These six volumes were registered and merged to obtain a high-definition OCTA volume. A projection-resolved OCTA algorithm was applied to suppress projection artifacts throughout the entire volume.[36,37] The internal limiting membrane, inner plexiform layer, inner nuclear layer (INL), outer plexiform layer, and Bruch's membrane were segmented by a guided bidirectional graph search algorithm.[38] Expert graders manually corrected errors on these layers' segmentation.

Multiple Three-Dimensional OCT/OCTA Volumetric Registration

We developed a volumetric registration algorithm to register and average six OCTA volumes to generate a high-definition OCTA volume. In this algorithm, we first generated en face OCTA from all the repeated scans. The en face OCTA with the highest signal strength index in all repeated scans served as the fixed image (Fig. 1A) to which the other scans were registered (Fig. 1B). Then, an intensity-based automated image registration algorithm was used to register these moving images with the fixed image.[38,39] The registration algorithm can produce transformation matrixes, which contain translation, rotation, and scaling parameters (Fig. 1C). These transformation matrixes were applied to the whole OCT/OCTA volumes for the scans to be registered (Fig. 1D). Thus each pair of C-scans between fixed and all moving scans were separately registered. Then, a normalized correlation method was deployed on each pair of A-lines in the fixed and moving cross-sections (Fig. 1E) to generate the registered volumes (Fig. 1F). Finally, these registered OCT/OCTA volumes were averaged to produce a high-definition volume (Fig. 1G).

Projection of En Face OCT/OCTA

Intermediate capillary plexus (ICP) angiograms were projected in a slab between the outer 20% of the ganglion cell complex and the inner 50% of the INL. We used redefined boundaries of deep capillary plexus (DCP) to project en face OCT/OCTA (Fig. 2). En face OCT/OCTA of DCP were projected in a slab 9 μm above the lower boundary of the INL and 12 μm below the lower boundary of the INL. En face OCT and OCTA of ICP and DCP were produced by mean and maximum projection of the OCT and OCTA signal,[40] respectively. In the FAZ, the en face OCT of DCP may contain hyperreflective spots (arrowhead position in Fig. 2B), which can greatly reduce the image contrast; moreover, pupil vignetting and the averaging of multiple repeated scans also can reduce the quality of en face OCT at the margin area. Thus a 0.6 mm radius circle centered over the fovea was excluded. An annular zone surrounded by a concentric ring 0.6 to 1.5 mm from the fovea was used to characterize deep capillaries (Fig. 2).

En Face OCT/OCTA Denoising

NPCs can be detected by comparing the OCT/OCTA images. However, the reflectance of capillaries and surrounding tissue significantly reduces the contrast in en face OCT, making it challenging to differentiate capillaries from tissue. In this study, we used en face OCTA, which have relatively less noise, to train a deep learning denoising model
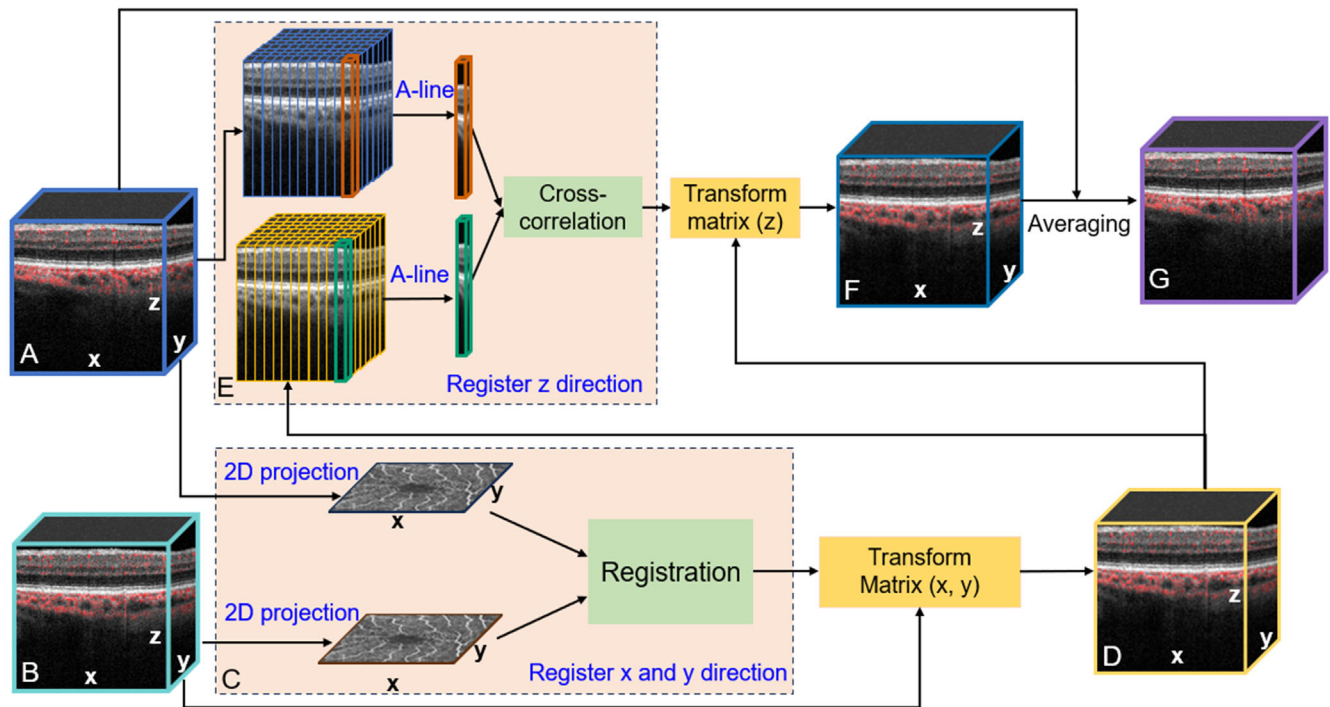
FIGURE 1. **(A)** Fixed OCTA volume. **(B)** Moving OCTA volume. **(C)** Registering moving angiogram with fixed angiogram and applying transform matrix to OCT/OCTA volumes. **(D)** Moving OCT/OCTA volume registered in the x- and y-directions. **(E)** Registering each pair of A lines in OCT volumes and applying the transform matrix to OCT/OCTA volumes. **(F)** Moving OCT/OCTA volumes registered in the z-direction. **(G)** Averaging the fixed and registered moving OCT/OCTA volumes to generate high-definition OCT/OCTA volumes.

and applied this model to en face OCT.[41] We used the denoised en face OCT/OCTA to generate the binary en face OCT/OCTA to segment NPCs.

An End-to-End Network Architecture

We designed an end-to-end convolutional neural network to generate background noise-resolved and enhanced en face OCTA of the intermediate and deep retinal slabs. The OCT angiograms (Fig. 3A) with different noise levels were input into the network to train a model. The ground truth was the reconstructed noise-free and high-definition angiograms generated from DCARnet, our previously validated denoising network.[29] The current network comprises a pyramid network (Fig. 3B) with dense block (Fig. 3C) and selective kernel subnetworks (SKNet) (Fig. 3D).[42] The pyramid network can provide multi-scale information using a hierarchical architecture. The features from the different scales were extracted by the dense block, which encourages the network to reuse features learned by earlier layers in the subsequent layers. This can be highly beneficial for feature extraction and learning representations, as it helps combat the vanishing gradient problem and promotes feature reuse. SKNet can improve the ability of convolutional neural network to capture multi-scale information by selectively integrating kernels with different receptive field sizes and resolutions, allowing the network to extract both local and global information in the input. Finally, the selected useful features from the different scales were fused to the output layer to generate noise-free en face OCTA (Fig. 3E). The ReLU activation function was used in each convolutional layer, except for the last convolution output layer.

Subjects and Ground Truth Generation for En Face OCTA Denoising

Each eye was repeatedly scanned using a 3×3 mm scan pattern centered on the macula (Fig. 4A). Among these multiple repeated scans, those exhibiting high motion artifacts and those that were off-center were excluded. Many studies have also shown that averaging of multiple en face OCTA can enhance image quality.[43,44] Registered and averaged OCT/OCTA volumes significantly suppressed the noise and improved the contrast and vascular connectivity (Fig. 4B). We selected 36 scans from 78 averaged scans from 78 eyes with AMD, ensuring low noise and high quality, to serve as the training dataset. In a previous study, we proposed DCARnet to reconstruct relatively low-resolution 6×6 mm en face OCTA using high-resolution 3×3 mm en face OCTA. This method does not generate false signals when the noise intensity is not extremely high.[29] Therefore we applied DCARnet (Fig. 4C) to these 36 scans to produce noise-free en face OCTA, which were used as the ground truth (Fig. 4D).

Training Parameters

The angiograms were reconstructed by DCARnet to generate the ground truth using 36 scans, which were registered and averaged from a total of 257 scans from 36 eyes. To enhance the ability of our network to remove strong noise from angiograms, we obtained the noise in the en face OCTA by subtracting the ground truth from the original angiograms of single and averaged scans. We then added 0 to 0.5 times of the real noise, in intervals of 0.1, to the original single and averaged angiograms to generate angiograms with varying
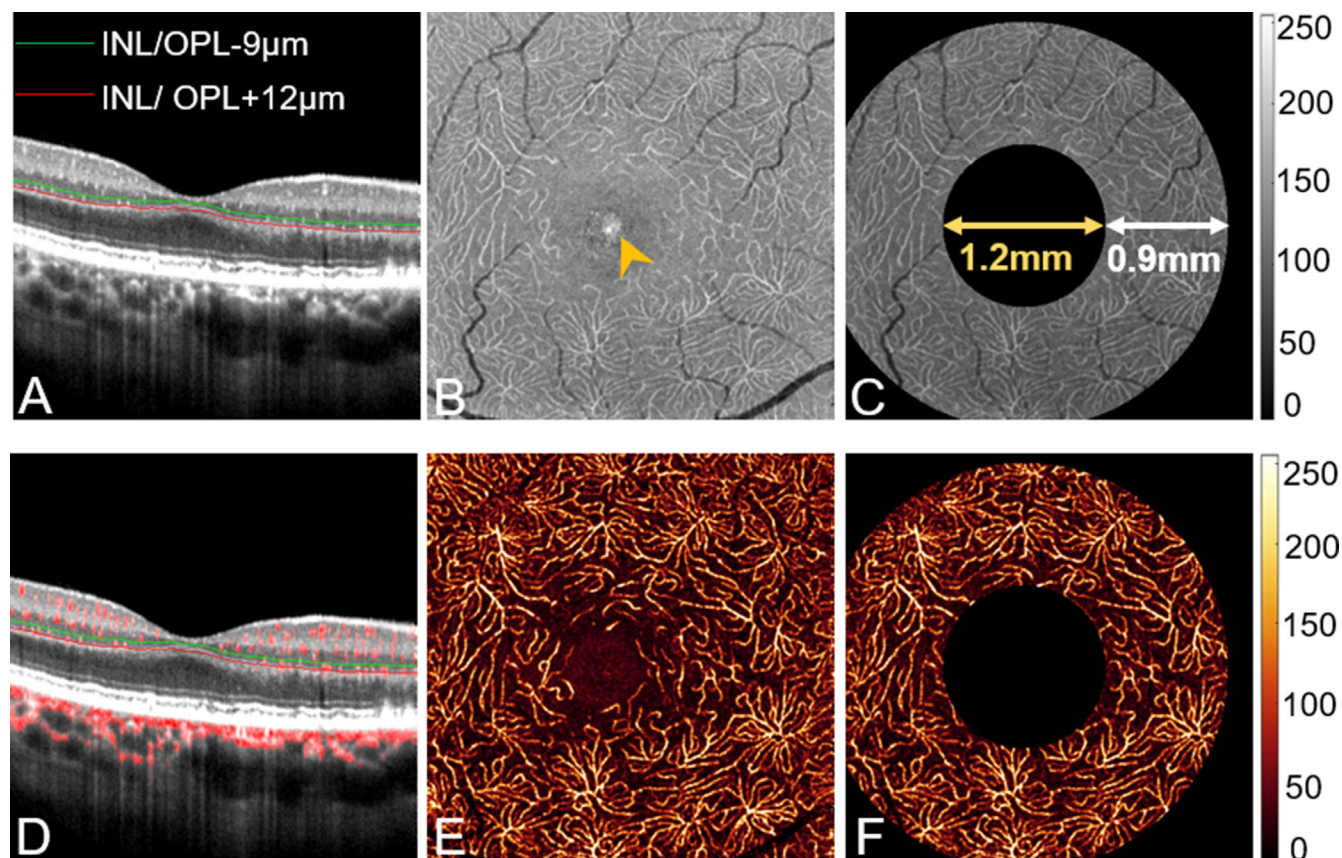
FIGURE 2. OCT/OCTA images of deep capillaries from an advanced AMD eye. **(A)** The DCP on cross-sectional OCT. The upper (*green curve*) and lower (*red curve*) boundaries of the region containing capillaries in DCP are indicated. **(B)** En face OCT of DCP using mean projection. **(C)** An annular zone surrounded by concentric rings 0.6 mm to 1.5 mm from the fovea was used to characterize capillaries due to strong noise and low contrast. **(D)** OCTA signal overlaid on cross-sectional OCT. **(E)** En face OCTA of DCP by maximum projection. **(F)** An annular zone of the OCTA signal was cropped for analysis.

noise intensities as network inputs. We also applied a flat-field correction to the original angiograms to reduce shading distortion and darkening. The correction uses Gaussian smoothing with a standard deviation of 30 to approximate the shading component of the angiogram. The illumination-compensated en face OCTA were also input to train the network.

To further augment our training data, we also included ICP angiograms as input, given the similarity between ICP and DCP features. The dataset was also augmented through horizontal and vertical flipping, random rotation and transposition, and random cropping. This resulted in the generation of 4102 ICP and DCP angiograms with different noise intensities. The training dataset comprised 3276 ICP and DCP angiograms, while the validation dataset consisted of 826 ICP and DCP angiograms.

The size of input images was 320×320 pixels, and the batch size was set to 4. We trained the network using the Adam optimizer with an initial learning rate of 0.0001 and a global learning rate decay strategy. Training was conducted on a GPU server equipped with four NVIDIA GeForce RTX 3090 graphics cards, using two of these cards for this study. The network was trained using a linear combined loss function incorporating mean square error and structural similarity.

Applying the OCTA Denoising Model to OCT and NPC Segmentation

To resolve background noise of the original en face OCT (Fig. 5A), we first adjusted the grayscale histogram to match[45] that of the en face OCTA (Fig. 5B), which served as the reference image. Then, a flat-field correction[46] was applied to the histogram matched en face OCT to reduce shading distortion and darkening (Fig. 5D). The correction uses Gaussian smoothing with a standard deviation of 30 to approximate the shading component of en face OCT. This adjustment enhanced the contrast of the en face OCT, producing capillary features similar to those in the en face OCTA (Fig. 5B). Thus we were able to apply the deep learning OCTA denoising model to the en face OCT. The deep learning model output noise-free en face OCT/OCTA (Figs. 5E, 5F), which were then binarized (Figs. 5G, 5H) and fused (Fig. 5I). NPCs (Fig. 5J) were generated by subtracting the flow signal identified by OCTA from the structural capillaries detected by OCT.

Evaluation and Characteristics of NPCs

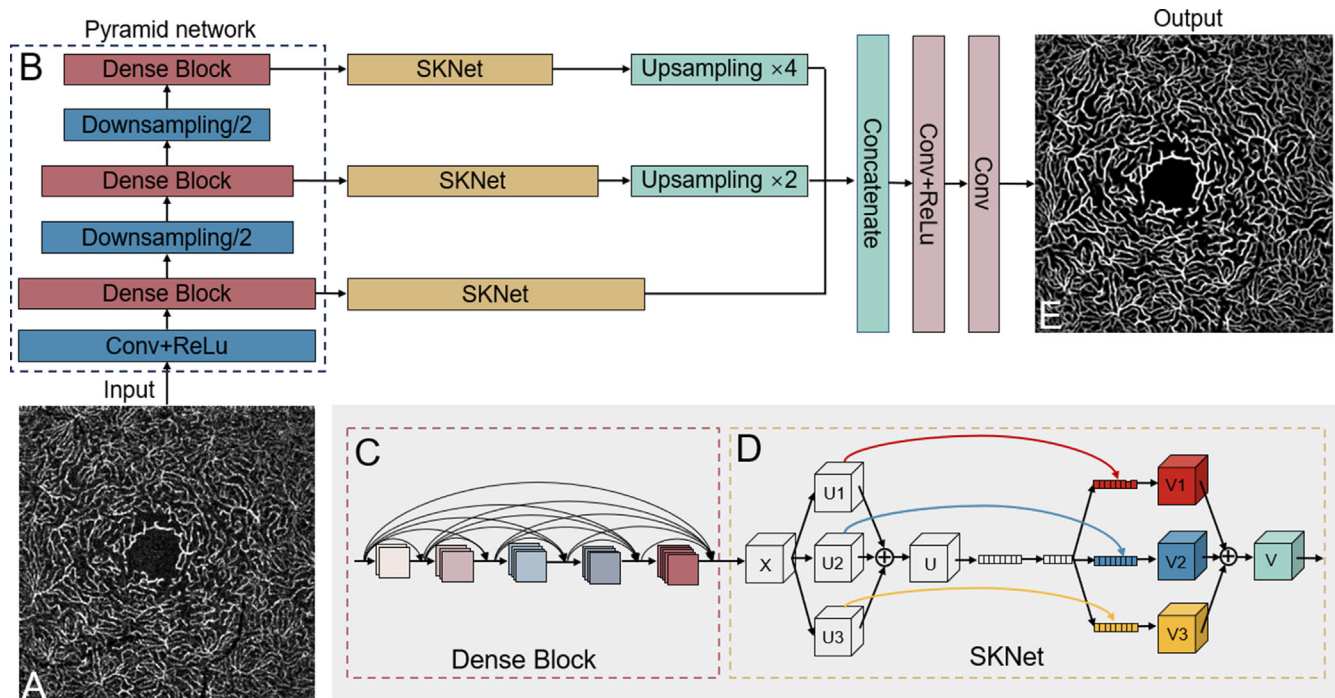The identification of NPCs is based on the difference between en face OCT (Figs. 6A, 6B) and OCTA (Figs. 6C, 6D).

FIGURE 3. Network architecture for en face OCTA denoising and enhancement. **(A)** The input is en face OCTA with different noise intensities. This en face OCTA **(A)** is from an early AMD eye. The input was downsampled a different number of times using a pyramid structure **(B)**, and features were extracted by a dense block **(C)** to pass to the SKNet **(D)**. SKNet fused features from the effective receptive fields of different kernel sizes using softmax attention in each scale. The effective features in each scale were selected and concatenated to output noise-free en face OCTA **(E)**.
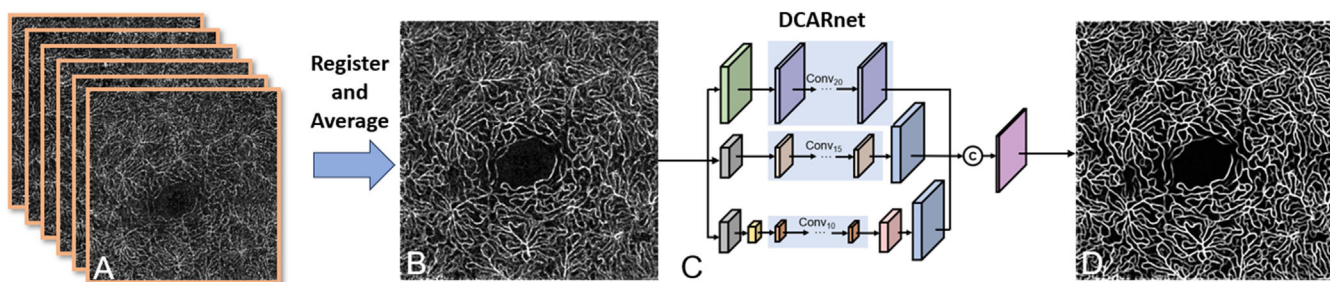

FIGURE 4. Multiple single OCT/OCTA scans **(A)** from an early AMD eye were registered and averaged to generate an OCT/OCTA volume. **(B)** En face OCTA of ICP and DCP were delivered to DCARnet. **(C)** to reconstruct a noise-free background image for an enhanced ground truth **(D)**.

Since the huge difference of signal intensity and signal noise ratio between two imaging modalities (Figs. 6E, 6F), comparing the difference between them is challenging. Generating ground truth for NPCs will consume huge amounts of time and resources. Our algorithm enhanced the signal-to-noise ratio and made the signal distribution pattern consistent to extract NPCs (Fig. 6I) from OCT (Fig. 6G) and OCTA (Fig. 6H). We chose empirically a length threshold of 75 µm for NPCs to filter out most noise segments while retaining the majority of NPCs. It is important to note that numerous discontinuous capillary structures observed on OCT may represent vertical vessels. To evaluate the accuracy of the identification of NPCs, two graders (Y.G., M.G.) first manually verified all segmented NPCs by first confirming they were real capillaries on en face OCT, then examined whether these real capillaries exhibited flow on OCTA. The accuracy

is defined by the percentage of the number of correct identified NPCs to the total number of identified NPCs.

We calculated the number and length of NPCs after skeletonization and compared them in healthy eyes and eyes with diseases, including AMD and DR. We specifically investigated whether significant differences existed in NPCs between varying severities of AMD. We explored the relationship between the number and length of NPCs and known features of AMD or DR, including GA, MNV, retinal fluid, drusen, extrafoveal avascular area (EAA), and microaneurysm. Retinal fluid, drusen, EAA, and GA were automatically segmented using deep learning-based methods.[3,5,10,13] Microaneurysms are defined as the oval shaped lesions with hyperreflective walls and dark lumens on cross-sectional OCT images.[4,47,48] Two ophthalmologists (T.H., S.B.) manually graded the presence of MAs and MNV.
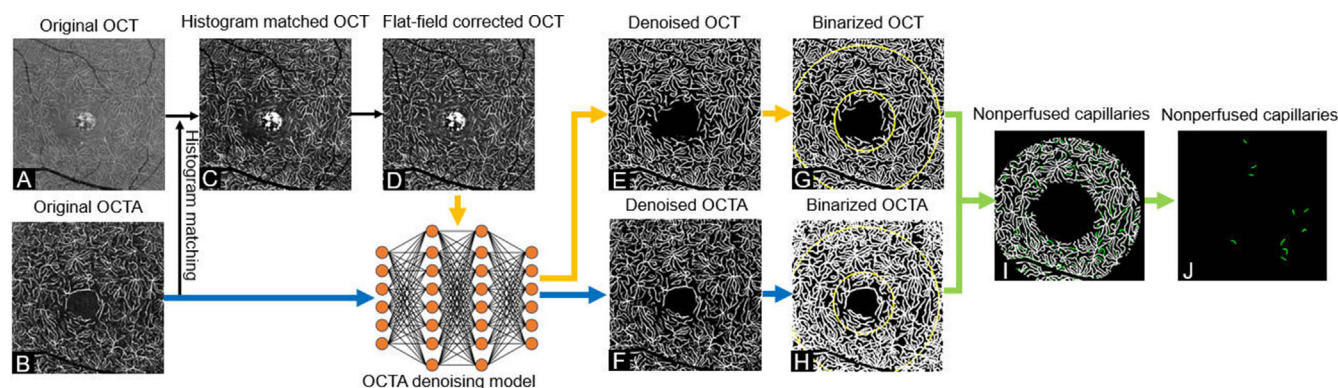
FIGURE 5. The nonperfused retinal capillaries (NPCs) segmentation in an eye with advanced AMD. **(A)** Original en face OCT. **(B)** Original en face OCTA. **(C)** The histogram of en face OCT was matched with that of en face OCTA, which served as the reference image. **(D)** Then a flat-field correction was applied to the histogram matched en face OCT to reduce shading distortion and darkening. The flat-field corrected en face OCT has similar features to original en face OCTA. The processed en face OCT **(D)** and original en face OCTA **(B)** were input to the trained OCTA denoising model to generate noise-resolved en face OCT/OCTA **(E, F)**. The denoised en face OCT and OCTA were binarized **(G, H)** and fused **(I)**, and then NPCs **(J)** were generated by subtracting the flow signal identified by OCTA from the structural capillaries detected by OCT.
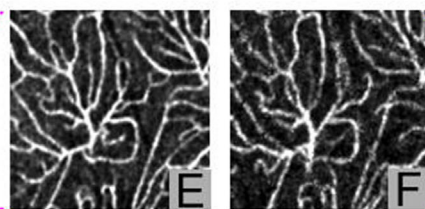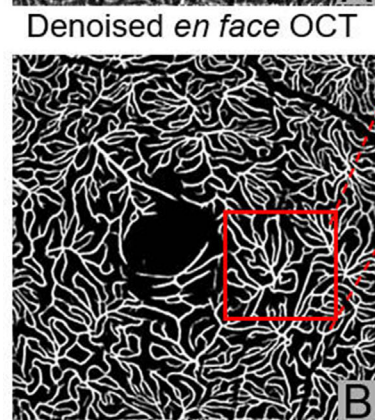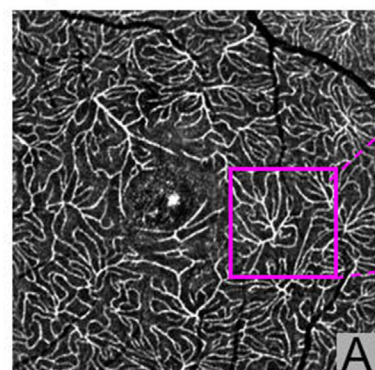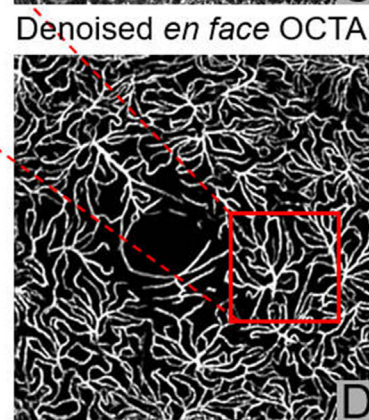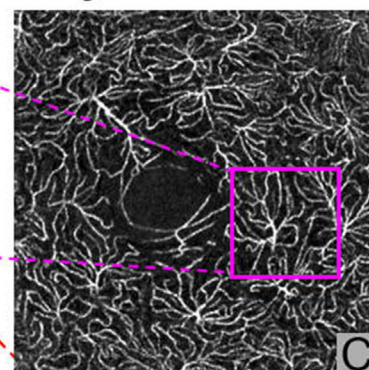

FIGURE 6. Identification of NPCs. **(A)** Adjusted en face OCT. **(B)** Noise-free en face OCT generated using deep learning-based denoising. **(C)** Original en face OCTA. **(D)** Denoised en face OCTA. **(E, F)** Enlarged regions from en face OCT and OCTA, respectively. **(G, H)** Corresponding enlarged regions after denoising. **(I)** Identification of NPCs by comparing en face OCT and OCTA.

Statistical Analysis

We first performed a Kolmogorov-Smirnov test to check if measurements were normally distributed. Then a Mann-Whitney U test was applied to test if there is a difference between two groups at a 5% significance level. For comparisons involving more than two groups, we used the Kruskal-Wallis test to assess whether at least one pair of groups showed significant differences. When significant differences were identified, Dunn's post hoc tests with Bonferroni correction were performed to determine which specific group pairs had statistically significant differences. Pearson

correlation coefficient was calculated to test the relationship between two continuous variables. Univariate logistic regression was used to suggest the relationship between the presence of a biomarker and the number or length of NPCs.

RESULTS

Clinical Characteristics of Study Participants

The clinical characteristics of study participants included healthy controls ($N = 43$), patients with AMD ($N = 78$), and those with mild to moderate NPDR ($N = 33$) (Table 1). The mean ages for the groups were 45.9 ± 17.5 years for the healthy controls, 77.1 ± 7.5 years for the AMD group, and 64.1 ± 11.6 years for the mild to moderate NPDR group. The number and length of NPCs did not show dependency on age in healthy controls. The number and length of NPCs in healthy eyes and eyes with AMD and DR were not normally distributed ($P < 0.05$, Kolmogorov-Smirnov test). Compared to healthy controls, both the number and length of NPCs significantly increased in eyes with AMD and mild to moderate NPDR ($P < 0.001$, $P < 0.001$, Mann-Whitney U test).

Performance of NPC Segmentation

Our method segmented 654 NPCs in 33 eyes with mild to moderate NPDR. However, because of the presence of very strong noise with high signal intensity and structures resem-

bling capillaries in en face OCT, 77 segments were erroneously detected as NPCs. The accuracy of NPC segmentation was 88.2% compared to manual graders. The segmented NPCs were further validated by examining the reflectance and flow signal on cross-sectional OCT/OCTA.

Relationship Between NPCs and Known Biomarkers in Eyes With AMD

Nonperfused retinal capillaries in 78 eyes with AMD (32 early AMD, 16 intermediate AMD, and 30 advanced AMD) were automatically segmented. The number and length of NPCs in early, intermediate and advanced AMD were not normally distributed ($P < 0.05$, Kolmogorov-Smirnov test). There were no significant differences in the number and total length between early and intermediate AMD (number: 11.12 ± 0.83 vs. 12.44 ± 1.22, $P = 0.492$; total length [mm]: 1.81 ± 1.83 vs. 2.13 ± 0.26, $P = 0.428$, post hoc test with Bonferroni correction). However, compared to eyes with early AMD, both the number and total length significantly increased in eyes with advanced AMD (number: 11.12 ± 0.83 vs. 26.27 ± 3.26, $P < 0.001$; total length [mm]: 1.81 ± 1.83 vs. 2.13 ± 5.39, $P < 0.001$). The number and total length of NPCs was also significantly higher in advanced AMD compared to intermediate AMD (number: 12.44 ± 1.22 vs. 26.27 ± 3.26, $P = 0.002$; total length [mm]: 2.13 ± 0.26 vs. 2.13 ± 5.39, $P = 0.003$). The presence of MNV ($N = 14$) and GA ($N = 21$) (Fig. 7A) was associated with both the number (odds ratio

TABLE 1. Clinical Characteristics of Study Participants With AMD, DR, and Controls

Parameters	Healthy Controls ($N = 43$)	AMD ($N = 78$)	Mild to Moderate NPDR ($N = 33$)
Age (mean $\pm$ SD)	45.9 ± 17.5	77.1 ± 7.5	64.1 ± 11.6
Sex			
Male	22	31	19
Female	21	47	14
Hypertension			
Yes	0	43	20
No	43	35	13
Diabetes			
Yes	0	9	33
No	43	69	0
Number of NPCs	1.79 ± 1.42	17.50 ± 13.12	19.82 ± 8.95
Total length of NPCs (mm)	0.35 ± 0.40	3.30 ± 3.34	5.63 ± 2.98

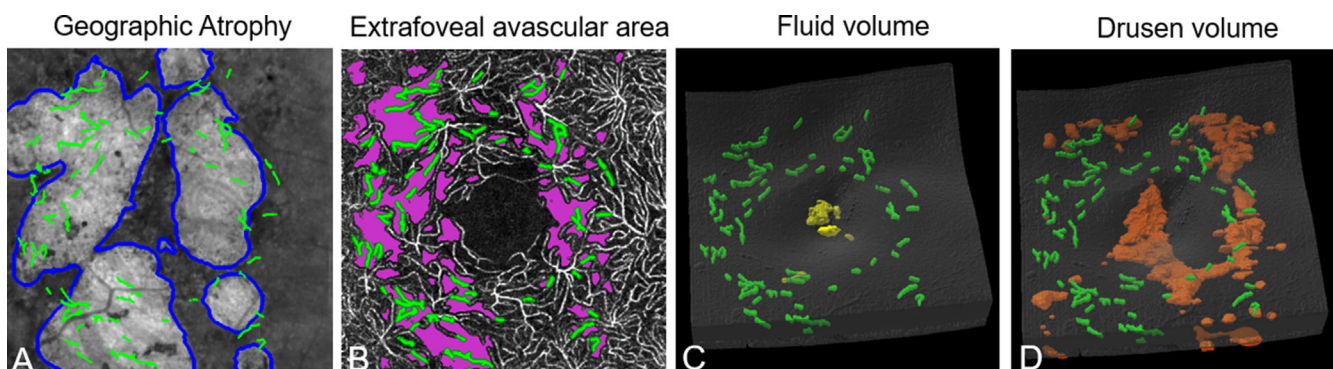NPCs, nonperfused retinal capillaries.

FIGURE 7. NPCs and known biomarkers in an eye with advanced AMD. **(A–D)** GA (*blue contour*), EAA (*violet*), fluid (*yellow*) and drusen (*orange*) volume were automatically segmented using deep learning-based methods. The presence of GA, NPA, and drusen volume significantly correlated with the number and total length of NPCs; however, the presence of retinal fluid was not related to either the number or total length of NPCs.

TABLE 2. Relationship Between NPCs and Known Biomarkers in Eyes With AMD ($N = 78$)

|	MNV Presence ($N = 14$)	GA Presence ($N = 26$)	Fluid Presence ($N = 19$)	EAA ($N = 78$)	Drusen Volume ($N = 78$)
Number of NPC	$^*P = 0.02$, OR = 1.07	$^*P < 0.001$, OR = 1.23	$^*P = 0.70$, OR = 1.01	$^{**}P < 0.001$, R = 0.55	$^{**}P = 0.02$, R = 0.27
Total length of NPC (mm)	$^*P = 0.02$, OR = 1.17	$^*P = 0.001$, OR = 1.62	$^*P = 0.46$, OR = 1.05	$^{**}P < 0.001$, R = 0.57	$^{**}P = 0.02$, R = 0.26

* Univariate logistic regression.
** Pearson correlation. Correlation is significant at 0.05.

TABLE 3. Relationship Between NPCs and Known Biomarkers in Eyes With Diabetic Retinopathy ($N = 33$)

	Fluid Presence ($N = 18$)	Number of Microaneurysm	Extrafoveal Avascular Area
Number of NPC	$^*P = 0.10$, OR = 1.07	$^{**}P = 0.03$, R = 0.37	$^{**}P < 0.001$, R = 0.72
Total length of NPC (mm)	$^*P = 0.08$, OR = 1.27	$^{**}P = 0.01$, R = 0.46	$^{**}P < 0.001$, R = 0.57

* Univariate logistic regression.
** Pearson correlation. Correlation is significant at 0.05.
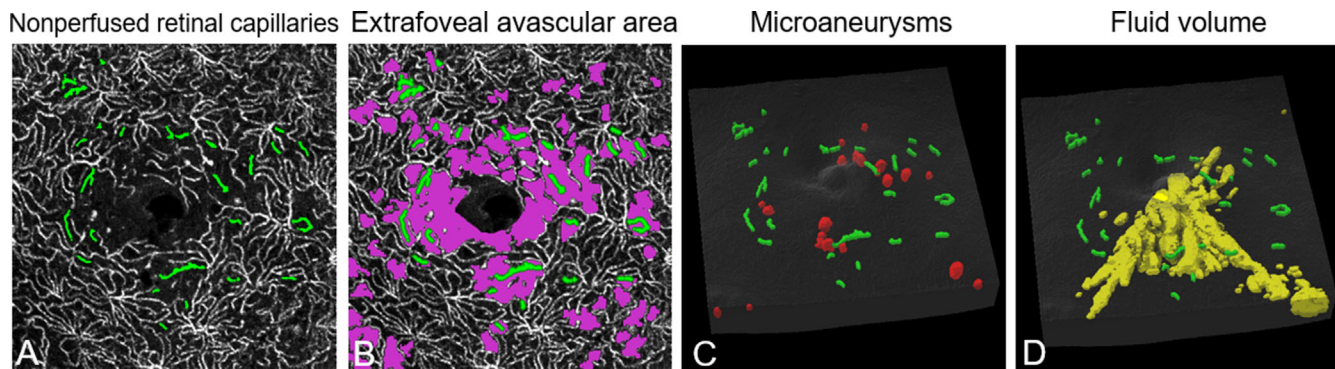
FIGURE 8. NPCs and known biomarkers in an eye with moderate nonproliferative diabetic retinopathy. **(A–D)** NPCs (*green*), EAA (*violet*), microaneurysms (*red*), and fluid (*yellow*) volume were automatically segmented using deep learning-based methods. The number of microaneurysms and NPA significantly correlated with the number and total length of NPCs; however, the presence of retinal fluid was not related to either the number or total length of NPCs.

[OR] = 1.227, $P < 0.001$; OR = 1.070, $P = 0.016$, univariate logistic regression) and the total length (OR = 1.624, $P = 0.001$; OR = 1.172, $P = 0.017$, univariate logistic regression) of NPCs (Table 2), with most NPCs situated within the GA region. The number and total length of NPCs showed no significant difference between eyes with only GA ($N = 9$) and those with only MNV ($N = 16$) ($P = 0.388$, $P = 0.329$, Mann-Whitney U test). EAA and drusen volume were related to the number ($R = 0.554$, $P < 0.001$; $R = 0.254$, $P = 0.025$, Pearson correlation) and total length ($R = 0.566$, $P < 0.001$; $R = 0.237$, $P = 0.037$, Pearson correlation) of NPCs (Figs. 7B, 7D) and the majority of NPCs were located within avascular areas (Fig. 7B). However, the presence of retinal fluid ($N = 19$) was not related to either the number ($P = 0.70$, OR = 1.01, univariate logistic regression) or the total length ($P = 0.46$, OR = 1.05, univariate logistic regression) of NPCs (Fig. 7C).

Relationship Between NPCs and Known Biomarkers in Eyes With Mild to Moderate NPDR

We segmented NPCs in 33 eyes with mild to moderate NPDR. The results showed that the number of microaneurysms were associated with the number ($P = 0.03$, $R = 0.37$, Pearson correlation) and total length ($P = 0.01$, $R = 0.46$, Pearson correlation) of NPCs (Table 3). NPCs were frequently located adjacent to microaneurysms (Fig. 8C). EAA was also correlated with the number ($P < 0.001$, $R = 0.72$, Pearson correlation) and total length ($P < 0.001$, $R = 0.57$, Pearson correlation) of NPCs. Most NPCs were located within avascular areas (Figs. 8A, 8B). However, the presence of fluid (18/15) was unrelated to the number ($P = 0.10$, OR = 1.07, univariate logistic regression) and total length ($P = 0.08$, OR = 1.27, Univariate logistic regression) of NPCs (Fig. 8D).

DISCUSSION

In this study, we used co-registered OCT and OCTA to develop a novel method for the automatic segmentation and characterization of NPCs, leveraging deep learning techniques to enhance the accuracy and reliability of NPC detection. The number and length of NPCs are increased in various levels of AMD and DR, suggesting their potential as a valuable biomarker of disease.

It is straightforward to understand that one modality can reveal capillary structure (whether perfused or not), while another modality displays the blood flow within these capillaries. By fusing these images, we can effectively distinguish nonperfused (occluded) segments from perfused (nonoccluded) ones. Traditionally, visualizing capillary structures has required high-resolution modalities equipped with adap-

tive optics (AO), such as AO-SLO or AO-OCT, for in vivo imaging. Although prior studies have demonstrated the use of commercial OCT for visualizing the innermost capillary loops at the FAZ border,[19] this visualization was limited to a small cohort of DR cases without the interference of edema. This highlights the need for advanced techniques to extend beyond the FAZ loop and address the signal attenuation challenges posed by pathologies, such as retinal edema.

A significant challenge in visualizing capillaries beyond the FAZ loop with OCT is differentiating true capillary structures from background noise. Given that a single capillary is only 5-10 microns wide—smaller than the transverse resolution of commercial OCT—its reflectance signal can be obscured by the surrounding retinal tissues. Our approach overcomes this by implementing four key steps.

First, we enhanced image resolution and contrast by improving signal-to-noise ratio using advanced three-dimensional registration and averaging techniques. Second, we carefully defined the study slab to further enhance the contrast between capillaries and the strong tissue background noise. Third, we developed a deep learning-based algorithm to denoise angiograms and applied it to eliminate the background tissue noise from en face OCT, revealing clear capillary structure and flow signal. Fourth, we used a multimodal fusion of OCT and OCTA images to combine structural and functional information, enabling precise identification of NPCs. These innovations collectively enhanced our ability to reveal capillary vasculatures, achieving a segmentation accuracy of 88.2%.

This approach was validated in cohorts with AMD and DR at Oregon Health and Science University, revealing significant correlations between NPCs and known biomarkers. Key findings from our results include:

- Compared to early and intermediate AMD, both the number and total length of NPCs were significantly increased in advanced AMD. These findings indicate a progression in the extent of NPCs as AMD advances to more severe stages.
- In both AMD and DR, the majority of NPCs were located within avascular areas (Figs. 7 and 8). This observation confirms our detection accuracy, as clusters of NPC segments form avascular regions.
- In AMD, the presence of GA was highly associated with NPCs, with most NPCs situated within the GA region (Fig. 7). This finding aligns with previous research indicating reduced retinal vessel density in the deep capillary plexus and significant loss within GA regions.[9]
- In exudative AMD, we found a significant association between MNV and NPC. This is consistent with our prior finding, which demonstrated larger extrafoveal avascular areas in the DCP in exudative AMD.[23]
- In DR, NPCs were frequently adjacent to microaneurysms, and the number of microaneurysms showed a strong correlation with NPC metrics. This is consistent with post-mortem histological observations by Cogan et al.,[20,49] who noted the localization of microaneurysms near zones of acellular, occluded capillaries in the early stages of DR. They speculated that capillary occlusion in these zones plays a critical role in the development and orientation of microaneurysms, accounting for the clustered and circular arrangement of lesions observed ophthalmoscopically in DR.
- Interestingly, retinal fluid did not exhibit a significant relationship with NPC metrics in either disease,

suggesting that NPCs may be more closely related to structural and vascular changes rather than fluid accumulation.

Despite these findings, there are several limitations to this study. First, multiple repeated scans are required for registration and averaging to improve scan contrast due to the low signal-to-noise ratio of a single OCT volume. This process is essential for extracting structural capillaries from OCT and identifying NPCs using co-registered OCTA. However, acquiring multiple repeated scans prolongs the total acquisition time, increasing the likelihood of image artifacts caused by eye movements and introducing additional challenges for clinical imaging workflow. With the rapid advancements in OCT technology, we anticipate that this limitation will be mitigated soon. For instance, ultrahigh-resolution OCT[50,51] will reduce the number of scans needed, and higher-speed OCT will reduce the acquisition time. Second, the study cohort is relatively small. In future research, increased patient enrollment will allow for the collection of more data, enabling a more comprehensive study of NPCs.

In conclusion, a new method was developed to segment and quantify NPCs using co-registered OCT and OCTA modalities. Our study demonstrates the potential of advanced imaging techniques and deep learning models to transform the detection and characterization of NPCs in retinal diseases.

References

1. Huang D, Swanson EA, Lin CP, et al. Optical coherence tomography. *Science*. 1991;254(5035):1178–1181.
2. Jia Y, Tan O, Tokayer J, et al. Split-spectrum amplitude-decorrelation angiography with optical coherence tomography. *Opt Express*. 2012;20:4710–4725.
3. Guo Y, Hormel TT, Xiong H, Wang J, Hwang TS, Jia Y. Automated segmentation of retinal fluid volumes from structural and angiographic optical coherence tomography using deep learning. *Transl Vis Sci Technol*. 2020;9(2):54.
4. Gao M, Hormel TT, Guo Y, et al. Perfused and nonperfused microaneurysms identified and characterized by structural and angiographic OCT. *Ophthalmol Retina*. 2024;8:108–115.
5. Guo Y, Camino A, Wang J, Huang D, Hwang TS, Jia Y. MEDnet, a neural network for automated detection of avascular area in OCT angiography. *Biomed Opt Express*. 2018;9:5147–5158.

Investigative Ophthalmology & Visual Science

6. Guo Y, Hormel TT, Xiong H, et al. Development and validation of a deep learning algorithm for distinguishing the nonperfusion area from signal reduction artifacts on OCT angiography. *Biomed Opt Express*. 2019;10:3257–3268.

7. Guo Y, Hormel TT, Gao L, et al. Quantification of nonperfusion area in montaged widefield OCT angiography using deep learning in diabetic retinopathy. *Ophthalmol Sci*. 2021;1(2):100027.

8. Guo Y, Hormel TT, Gao M, et al. Multi-plexus nonperfusion area segmentation in widefield OCT angiography using a deep convolutional neural network. *Transl Vis Sci Technol*. 2024;13(7):15–15.

9. You QS, Wang J, Guo Y, et al. Detection of reduced retinal vessel density in eyes with geographic atrophy secondary to age-related macular degeneration using projection-resolved optical coherence tomography angiography. *Am J Ophthalmol*. 2020;209:206–212.

10. Guo Y, Hormel T, Gao M, Hwang TS, Bailey ST, Jia Y. A deep learning-based method for retinal layer and drusen segmentation on optical coherence tomography. *Invest Ophthalmol Vis Sci*. 2022;63(7):3001–F0271.

11. Hu Z, Medioni GG, Hernandez M, Hariri A, Wu X, Sadda SR. Segmentation of the geographic atrophy in spectral-domain optical coherence tomography and fundus autofluorescence images. *Invest Ophthalmol Vis Sci*. 2013;54(13):8375.

12. Wang M, Zhu W, Shi F, et al. MsTGANet: automatic drusen segmentation from retinal OCT images. *IEEE Trans Med Imaging*. 2022;41:394–406.

13. Guo Y, Hormel TT, Gao M, Bailey ST, Jia Y. Geographic Atrophy Segmentation On Optical Coherence Tomography. *Invest Ophthalmol Vis Sci*. 2024;65(9):PB0091–PB0091.

14. Wang J, Hormel TT, You Q, et al. Robust non-perfusion area detection in three retinal plexuses using convolutional neural network in OCT angiography. *Biomed Opt Express*. 2020;11:330.

15. Hwang TS, Jia Y, Gao SS, et al. Optical coherence tomography angiography features of diabetic retinopathy. *Retina*. 2015;35:2371–2376.

16. Hwang TS, Zhang M, Bhavsar K, et al. Visualization of 3 distinct retinal plexuses by projection-resolved optical coherence tomography angiography in diabetic retinopathy. *JAMA Ophthalmol*. 2016;134:1411.

17. Hwang TS, Hagag AM, Wang J, et al. Automated quantification of nonperfusion areas in 3 vascular plexuses with optical coherence tomography angiography in eyes of patients with diabetes. *JAMA Ophthalmol*. 2018;136: 929.

18. Jia Y, Bailey ST, Wilson DJ, et al. Quantitative optical coherence tomography angiography of choroidal neovascularization in age-related macular degeneration. *Ophthalmology*. 2014;121:1435–1444.

19. Green WR WDJ. Histopathology of diabetic retinopathy. In: Franklin RM, ed. *Retina and Vitreous: Proceedings of the Symposium on Retina and Vitreous*; Amsterdam, Netherlands: Kugler Publications; 1993:63–82.

20. Cogan DG, Kuwabara T. Capillary shunts in the pathogenesis of diabetic retinopathy. *Diabetes*. 1963;12:293–300.

21. Stefánsson E, Chan YK, Bek T, Hardarson SH, Wong D, Wilson DI. Laws of physics help explain capillary nonperfusion in diabetic retinopathy. *Eye*. 2018;32:210–212.

22. Curtis TM, Gardiner TA. Ocular blood flow in diabetes: contribution to the microvascular lesions of diabetic retinopathy. In: Schmetterer L, Kiel J, eds. *Ocular Blood Flow*. Berlin: Springer; 2012:367–388.

23. Gao L, Wang J, You Q, et al. Plexus-specific retinal capillary avascular area in exudative age-related macular degeneration with projection-resolved OCT angiography. *Br J Ophthalmol*. 2022;106:719–723.

24. Colantuono D, Souied EH, Borrelli E, et al. Quantitative deep vascular complex analysis of different AMD stages on optical coherence tomography angiography. *Eur J Ophthalmol*. 2021;31:2474–2480.

25. Lee SC, Tran S, Amin A, et al. Retinal vessel density in exudative and nonexudative age-related macular degeneration on optical coherence tomography angiography. *Am J Ophthalmol*. 2020;212:7–16.

26. Pinhas A, Razeen M, Dubow M, et al. Assessment of perfused foveal microvascular density and identification of nonperfused capillaries in healthy and vasculopathic eyes. *Invest Ophthalmol Vis Sci*. 2014;55:8056–8066.

27. Lynch G, Romo JSA, Linderman R, et al. Within-subject assessment of foveal avascular zone enlargement in different stages of diabetic retinopathy using en face OCT reflectance and OCT angiography. *Biomed Opt Express*. 2018;9:5982.

28. Gao M, Guo Y, Hormel TT, Sun J, Hwang TS, Jia Y. Reconstruction of high-resolution 6×6-mm OCT angiograms using deep learning. *Biomed Opt Express*. 2020;11: 3585.

29. Gao M, Hormel TT, Wang J, et al. An open-source deep learning network for reconstruction of high-resolution OCT angiograms of retinal intermediate and deep capillary plexuses. *Transl Vis Sci Technol*. 2021;10(13):13.

30. Yuan Z, Yang D, Wang W, Zhao J, Liang Y. Self super-resolution of optical coherence tomography images based on deep learning. *Opt Express*. 2023;31(17):27566.

31. Roy AG, Conjeti S, Karri SPK, et al. ReLayNet: retinal layer and fluid segmentation of macular optical coherence tomography using fully convolutional networks. *Biomed Opt Express*. 2017;8:3627.

32. Ronneberger O, Fischer P, Brox T. U-Net: Convolutional Networks for Biomedical Image Segmentation. In: *Lecture Notes in Computer Science (Including Subseries Lecture Notes in Artificial Intelligence and Lecture Notes in Bioinformatics)*. Cham: Springer; 2015; 9351:234–241.

33. Guo Y, Hormel TT, Pi S, et al. An end-to-end network for segmenting the vasculature of three retinal capillary plexuses from OCT angiographic volumes. *Biomed Opt Express*. 2021;12:4889.

34. Gao M, Guo Y, Hormel TT, et al. A deep learning network for classifying arteries and veins in montaged widefield OCT angiograms. *Ophthalmol Sci*. 2022;2(2):100149.

35. Kraus MF, Potsaid B, Mayer MA, et al. Motion correction in optical coherence tomography volumes on a per A-scan basis using orthogonal scan patterns. *Biomed Opt Express*. 2012;3:1182–1199.

36. Wang J, Zhang M, Hwang TS, et al. Reflectance-based projection-resolved optical coherence tomography angiography. *Biomed Opt Express*. 2017;8:1536–1548.

37. Wang J, Wang J, Hormel TT, et al. Signal attenuation-compensated projection-resolved OCT angiography. *Biomed Opt Express*. 2023;14:2040–2054.

38. Klein S, Staring M, Murphy K, Viergever MA, Pluim J. Elastix: a toolbox for intensity-based medical image registration. *IEEE Trans Med Imaging*. 2010;29:196–205.

39. Zang P, Liu G, Zhang M, et al. Automated three-dimensional registration and volume rebuilding for wide-field angiographic and structural optical coherence tomography. *J Biomed Opt*. 2017;22:026001.

40. Hormel TT, Wang J, Bailey ST, Hwang TS, Huang D, Jia Y. Maximum value projection produces better en face OCT angiograms than mean value projection. *Biomed Opt Express*. 2018;9:6412.

41. Gao M, Guo Y, Hormel T, Wang J, Hwang TS, Jia Y. Background noise-resolved and enhanced OCT angiography using an end-to-end convolutional neural network. *Invest Ophthalmol Vis Sci*. 2023;64:2365–2365.

Investigative Ophthalmology & Visual Science

42. Li X, Wang W, Hu X, Yang J. Selective kernel networks. In: *Proceedings of the IEEE/CVF Conference on Computer Vision and Pattern Recognition*; 2019:510–519.

43. Uji A, Balasubramanian S, Lei J, Baghdasaryan E, Al-Sheikh M, Sadda SR. Impact of multiple en face image averaging on quantitative assessment from optical coherence tomography angiography images. *Ophthalmology*. 2017;124:944–952.

44. Uji A, Balasubramanian S, Lei J, et al. Multiple enface image averaging for enhanced optical coherence tomography angiography imaging. *Acta Ophthalmol*. 2018;96(7):E820–E827.

45. Chourasiya A, Khare N. A comprehensive review of image enhancement techniques. *Int J Innovative Res Growth*. 2019;8(6).

46. Ruben G, Croton LCP, Paganin DM, Morgan KS, Kitchen MJ. Ring artifact suppression in X-ray computed tomography using a simple, pixel-wise response correction. *Opt Express*. 2019;27:14231–14245.

47. Horii T, Murakami T, Nishijima K, Sakamoto A, Ota M, Yoshimura N. Optical coherence tomographic characteristics of microaneurysms in diabetic retinopathy. *Am J Ophthalmol*. 2010;150:840–848.e1.

48. Wang H, Chhablani J, Freeman WR, et al. Characterization of diabetic microaneurysms by simultaneous fluorescein angiography and spectral-domain optical coherence tomography. *Am J Ophthalmol*. 2012;153:861–867.e1.

49. Cogan DG. Retinal vascular patterns. *Arch Ophthalmol*. 1961;66:366.

50. Chen S, Abu-Qamar O, Kar D, et al. Ultrahigh resolution OCT markers of normal aging and early age-related macular degeneration. *Ophthalmol Sci*. 2023;3(3):100277.

51. Patil A, Chakravorty C. Detection of hard exudate using retinal optical coherence tomography (OCT) images. *Global Transitions Proceedings*. 2021;2:566–570.